



## ISTITUTO NAZIONALE DI RICERCA METROLOGICA Repository Istituzionale

Assessment of Exposure to MRI Motion-Induced Fields  
Based on the International Commission on Non-Ionizing Radiation Protection (ICNIRP)

This is the author's submitted version of the contribution published as:

*Original*

Assessment of Exposure to MRI Motion-Induced Fields

Based on the International Commission on Non-Ionizing Radiation Protection (ICNIRP) Guidelines / Zilberti, Luca; Bottauscio, Oriano; Chiampi, M.. - In: MAGNETIC RESONANCE IN MEDICINE. - ISSN 0740-3194. - 76:4(2016), pp. 1291-1300. [10.1002/mrm.26031]

*Availability:*

This version is available at: 11696/29046 since: 2021-01-27T16:16:30Z

*Publisher:*

Wiley

*Published*

DOI:10.1002/mrm.26031

*Terms of use:*

This article is made available under terms and conditions as specified in the corresponding bibliographic description in the repository

*Publisher copyright*

WILEY

Optica Publishing Group under the terms of the Open Access Publishing Agreement. Users may use, reuse, and build upon the article, or use the article for text or data mining, so long as such uses are for noncommercial purposes and appropriate attribution is maintained. All other rights are reserved

(Article begins on next page)

# **Assessment of Exposure to MRI Motion-Induced Fields Based on the ICNIRP Guidelines**

Luca Zilberti,<sup>1</sup> Oriano Bottauscio,<sup>1</sup> Mario Chiampi<sup>2</sup>

<sup>1</sup>Istituto Nazionale di Ricerca Metrologica, Torino, Italy.

<sup>2</sup>Politecnico di Torino, Dipartimento Energia, Torino, Italy.

Correspondance to: Luca Zilberti, Istituto Nazionale di Ricerca Metrologica, Strada delle Cacce 91, I-10135, Torino, Italy. E-mail: l.zilberti@inrim.it

Word count: 4923

## **Abstract**

**Purpose:** The paper presents an exposure assessment for workers moving through the stray stationary field of common MRI scanners, performed according to the recent ICNIRP Guidelines, which aim at avoiding annoying sensory effects.

**Theory and Methods:** The analysis is carried out via numerical simulations, considering a high-resolution anatomical model, which moves along realistic trajectories in proximity to a tubular and an open MRI scanner. Both dosimetric indexes indicated by ICNIRP (maximum variation of the magnetic flux density vector and exposure index for the motion-induced electric field) are computed, considering three statures of the human model.

**Results:** 51 exposure situations are analyzed. None of them exceeds the limits for the maximum variation of the magnetic flux density, while some critical cases are found when computing the induced electric field. In this latter case, the exposure indexes computed via Fourier Transform and through an equivalent filter result to be consistent.

**Conclusion:** The results suggest the adoption of some simple precautionary rules, useful when the sensory effects experienced by the operators could reflect upon patients' safety. Moreover, some open issues regarding the quantification of motion-induced fields are highlighted, putting in evidence the need for clarification at standardization level.

**Keywords:** motion-induced electric field, static magnetic field, workers' safety

## INTRODUCTION

In March 2014 the International Commission on Non-Ionizing Radiation Protection (ICNIRP) published Guidelines (1) providing exposure limits to the “motion-induced fields”, i.e. electric fields induced in a body moving through a stationary magnetic field. This kind of exposure can give rise to annoying sensory effects (1-4), such as vertigo and nausea (5), metallic taste in the mouth (6), magnetophosphenes (visual flickering sensation) (7) and decrements in eye-hand coordination (8). These effects are transient and do not represent a direct danger for health, but they can impair working ability. Because of their diffusion and quite high stray fields, the attention of the dosimetric investigations has been focused on the rooms for Magnetic Resonance Imaging (MRI). There, a decrement in the performance of the medical staff could have repercussions on patients’ safety, limiting the development of MRI-guided therapies (9) or surgeries (10).

Some studies have quantified the magnetic field experienced by the operators experimentally (11) and the risk related to the exposure has been analyzed statistically (12). Since in-vivo measurements of induced quantities are unfeasible, most of the studies aimed at quantifying motion-induced fields relies on computations (13-24). However, none of these studies included the computation of the exposure indexes recently recommended by the ICNIRP Guidelines, which could become a legal requirement in the next future. This should happen, for instance, when putting into effect the European Directive 2013/35/EU (25). Such Directive was issued before the publication of the Guidelines (1); nevertheless, in Article 11, it comprises the specific provision: “The Commission shall adopt a delegated act, in accordance with Article 12, to insert into Annex II the ICNIRP guidelines for limiting exposure to electric fields induced by movement of the human body in a static magnetic field [...] as soon as they are available”. Thus, the ICNIRP Guidelines should be considered as an integral part of the Directive. It must be also noted that, in Article 10, the Directive allows derogations for the use of MRI systems, but access to this exemption may be obtained *provided that* a risk assessment has demonstrated that the exposure limits are exceeded (i.e. the exposure indexes have to be computed preliminarily, anyway).

This paper presents the results of an extensive exposure assessment, carried out via numerical simulations, applied to two MRI scanners: a traditional tubular scanner and an open scanner with vertical axis. The simulations makes use of a high-resolution anatomical model of the human body (assuming three possible statures, to extend the survey), moving along realistic trajectories. The analysis of the exposure is performed according to the rules provided in (1), i.e. computing the variation of the magnetic flux density vector (the metric to prevent vertigo) and the exposure index for the induced electric field (the metric to prevent magnetophosphenes and peripheral nerve stimulation, PNS). It must be noted that, in MRI practice, PNS is not generally experienced by people moving through the stationary magnetic field, but during the exposure to switched-gradient fields. Concerning this, ICNIRP itself states: “For normal movements, the threshold for peripheral nerve stimulation is unlikely to be reached with exposures below 8 T” (1). However, since motion-induced fields typically involves spectral harmonics above 1 Hz (regulated by the Guidelines published in 2010 (26), which include prescriptions for PNS), ICNIRP proposes to extend below 1 Hz the application of the basic restrictions set in (26). Omitting a discussion about the formulation of the exposure limits, which

goes beyond the scope of this work, the paper relies on the ICNIRP Guidelines (which, as already mentioned, are often taken as a legal requirement *de facto*) and focuses the attention on the assessment procedure.

## METHODS

### Human Model

The human body is represented through the Duke dataset (27), i.e. the model of an adult male including 77 tissues. The model has been segmented into cubic voxels with 4 mm side, and, since the assessment is focused on the head, it has been truncated just below the shoulders (preliminary computations showed that this operation does not introduce significant perturbations in the results inside the head). The overall dimensions of the model are 44.4 cm (height), 51.6 cm (width), 26.4 cm (depth); the total number of effective voxels is 264461. By changing the vertical position of the model, three versions are considered: model OM, which keeps the “original” stature ( $h = 1.77$  m), and other two additional models whose stature is decreased or increased of 15 cm (model SM, with  $h = 1.62$  m and model TM, with  $h = 1.92$  m). This operation extends the investigation to a shorter and a taller person, but it can be also interpreted as a change in the height of the MRI scanner with respect to the floor (keeping  $h = 1.77$  m). The conductivity of tissues has been extrapolated from the values provided in (28), applying a 4<sup>th</sup>-order Cole-Cole dispersion model for a frequency of 1 Hz. The permittivity of tissues has a low impact on the computations (24) and therefore it has been ignored.

### MRI scanners

The assessment is performed with reference to two MRI scanners, whose design has been provided by a manufacturer. The first one is a tubular scanner with its axis 98 cm above the floor, representative for a large part of the MRI scanners used in clinical applications. It operates with a stationary field of 3 T, which practically represents a worst-case when analyzing clinical tubular scanners. The second scanner is an open ironless tomograph with vertical axis, composed of two sets of coils separated by a 60 cm gap and the isocenter at 110 cm from ground, which operates at a nominal magnetic flux density equal to 1 T.

### Numerical models

The distributions of the magnetic flux density ( $\mathbf{B}$ ) and of a corresponding vector potential ( $\mathbf{A}$ ) are preliminarily computed around the tomographs, being known the magnetomotive force of each coil inside the scanners. During the simulations, the human model moves rigidly, following the trajectories described in the next paragraph. At each time instant, both  $\mathbf{B}$  and  $\mathbf{A}$  are determined for all voxels and projected on the local reference frame co-moving with the body. The maximum vectorial variation of the magnetic flux density over the whole motion,  $|\Delta\mathbf{B}|$ , is computed for each voxel and compared with the limit (2 T) for “uncontrolled conditions” (environments where access is not restricted to trained workers only).

The evolution of the Cartesian components of the induced electric field is computed, across time, through the potential-based Finite Element numerical scheme described in (24), where the time derivative of the vector potential, computed in the co-moving frame, is exploited as driving term. As a boundary condition, the normal

component of the induced current density is assumed to be null at the interface between the body and the external air. This condition is applied also where the human model has been truncated, having verified preliminarily that a lowering the truncation does not affect the results in the head significantly). The exposure evaluation is carried out for each voxel with reference to the limits set for uncontrolled conditions (i.e. the worst case) in (1), extended above 1 Hz to meet the limits provided by ICNIRP in the Guidelines devoted to low-frequency fields (26). In order to get a worst-case evaluation, above 1 Hz the basic restrictions have been chosen with reference to the occupational exposure of the central nervous system (CNS) of the head. The adopted exposure limits ( $EL$ ), expressed as peak values, change with frequency ( $f$ ) as follows:

- 1.1 V/m between 0 Hz and 0.66 Hz;
- $(0.7/f)$  V/m between 0.66 Hz and 1 Hz;
- $(\sqrt{2} \cdot 0.5/f)$  V/m between 1 Hz and 10 Hz;
- $(\sqrt{2} \cdot 0.05)$  V/m between 10 Hz and 25 Hz.
- $(\sqrt{2} \cdot 2 \cdot 10^{-3} \cdot f)$  V/m between 25 Hz and 400 Hz.

Frequencies higher than 400 Hz are not considered because irrelevant to motion-induced fields.

Since the induced electric field is a non-sinusoidal signal, the Guidelines (1) require quantifying the exposure according to the “weighted-peak approach” (26, 29). Such a technique has been implemented both in the version based on the Discrete Fourier Transform (DFT), working in frequency domain, and in the one which exploits a suitable digital filter, in time domain.

When adopting the DFT technique, the time-signal of each Cartesian component of the electric field is decomposed into the sum of  $N$  spectral harmonics. The generic  $i$ -th harmonic has a magnitude  $M_i$ , a frequency  $f_i$  and a phase  $\theta_i$ . Then, each harmonic is “compared” with the corresponding exposure limit ( $EL_i$ ). Finally, the contributions of all harmonics are aggregated in a cumulative way through a summation, obtaining a “weighted signal”  $WS$ :

$$WS(t) = \sum_i^N \frac{M_i}{EL_i} \cos(2\pi f_i t + \theta_i + \varphi_i) \quad [1]$$

Note that, in Eq. 1, the weighting of each harmonic is performed not only by dividing its magnitude by the exposure limit, but also by introducing a phase-shift  $\varphi_i$ . The values of  $\varphi_i$  are provided in Fig. 1, following the rules given in (26, 29).

For any computational point, Eq. 1, applied to the three Cartesian components of the field, provides the three corresponding weighted signals  $WS_x(t)$ ,  $WS_y(t)$ ,  $WS_z(t)$ , which are then reassembled via quadratic summation. The peak of the resulting function is adopted by ICNIRP as exposure index  $EI$  (which should be lower than 1 to comply with the limits):

$$EI = \max \left( \sqrt{WS_x^2 + WS_y^2 + WS_z^2} \right) \quad [2]$$

When using the filter technique, the weighted signals  $WS_x$ ,  $WS_y$  and  $WS_z$  are obtained as the output of a suitable filter, which receives in input the time-signals of the Cartesian components of the electric field. Then, the exposure index is computed through relation 2 as well. Of course, the transfer function of the filter must be

designed to approximate the weighting function adopted in Eq. 1 (i.e. the behavior of  $EL^{-1}$  and  $\varphi$  across frequency). By working in the realm of Laplace Transform (with complex angular frequency  $s$ ), in a first attempt such transfer function could be defined as:

$$F(s) = \frac{1}{1.1} \frac{\left(\frac{s}{2\pi 0.66} + 1\right) \left(\frac{s}{2\pi 400} + 1\right)}{\left(\frac{s}{2\pi 10} + 1\right) \left(\frac{s}{2\pi 25} + 1\right)} \quad [3]$$

where the two poles (at 10 Hz and 25 Hz) and the two zeros (at 0.66 Hz and 400 Hz) simply correspond to the frequency values where the “slope” of the limits given by ICNIRP changes. However, at some frequencies, the magnitude of  $F(s)$  diverges from  $1/EL$  more than 3 dB (compare the black and red curves in Fig.1a), i.e. the threshold that should not be exceeded to guarantee a good conformity to Eq. 1 (26). To reach a more satisfactory agreement, an “advanced” filter has been specifically designed. Its transfer function, whose magnitude diverges from  $1/EL$  less than 3 dB in the range between 0 - 30 Hz and, in particular, less than 1.5 dB in the range 0 - 10 Hz, is:

$$T(s) = \frac{1}{1.1} \frac{\left(\frac{s}{2\pi 0.75} + 1\right) \left(\frac{s}{2\pi 1} + 1\right) \left(\frac{s}{2\pi 2.1} + 1\right) \left(\frac{s}{2\pi 2.8} + 1\right)}{\left(\frac{s}{2\pi 0.67} + 1\right) \left(\frac{s}{2\pi 3.2} + 1\right) \left(\frac{s}{2\pi 5.5} + 1\right) \left(\frac{s}{2\pi 15} + 1\right) \left(\frac{s}{2\pi 18} + 1\right)} \quad [4]$$

As can be seen in Fig.1a,  $|T| > EL^{-1}$  for most of the considered frequency band.

Figure 1b shows the behavior of the phase angle associated to  $F(s)$  and  $T(s)$ , in comparison with the angle  $\varphi$  (defined according to (26)) to be used in Eq. 1. The phase angle of  $T(s)$  approximates  $\varphi$  better than the phase of  $F(s)$  and respect the maximum deviation allowed by the Guidelines (i.e.  $90^\circ$ ). However, it still deviates significantly from  $\varphi$ , mainly in correspondence to its discontinuities.

The spectra of motion-induced signals typically include a DC component, which represents an electric field, constant during the observation time window, directly applied *in situ* to the tissue. The Guidelines (1) do not prescribe explicitly how to treat this DC component and, in their table 1, provide basic restrictions starting from 0 Hz, leaving, in the authors’ opinion, an ambiguity about the inclusion of the DC component in the computation of the exposure index. For this reason, in the Results Section, the exposure index will be presented both including and excluding the DC component (note that, in Eq. 1, it can be easily taken into account by setting  $f = 0$ ,  $\varphi = 0$  and  $\theta = 0$  or  $\theta = 180^\circ$  for positive or negative DC components, respectively). However, the removal of the DC component must be done with due caution when filtering in time domain (see the Appendix for more details).

### Motion trajectories

Some realistic trajectories followed by the moving body are considered. Each trajectory is described by a trapezoidal speed (or angular speed, in case of rotation), including an acceleration phase, a phase of uniform motion and a final deceleration phase (with the same duration as for the acceleration) which brings the speed back to zero. Six translations (trajectories T1 to T6) and five rotations around the axis of the body (trajectories

T7 to T11) are investigated for the tubular scanner. For the open scanner, three translations (trajectories T12 to T14) and three rotations around the axis of the body (trajectories T15 to T17) are analyzed. A schematic top-view of the scanners is given in Figs. 2 and 3, where the light-blue rectangle indicates the space taken up by the coils (whose axis is directed along  $z$ , for both cases). The same figures provide a representation of the 17 trajectories, where the circles indicate the position of the model head (smaller than the model itself, which includes the shoulders). Since the dimension of a real scanner exceeds the volume taken up by the coils (because of the cryostat), all trajectories have been designed so that one part of the model (head/back/shoulder) can approach the external cover of the scanner, but without going over it. All trajectories could be covered in the opposite direction, keeping the values of the exposure indexes fairly unchanged (but not identical, due to the body asymmetries).

The details of all trajectories are summarized in Table 1. The coordinates of the starting and final points refer to the position of the axis of the body, expressed in the reference frames given in Fig.2 (for the tubular scanner, with the body axis parallel to the  $y$ -axis) and Fig.3 (for the open scanner, with the body axis parallel to the  $z$ -axis). In summary:

- Trajectories T1 and T12 are translations crossing the direction of the examination couch.
- Trajectories T2 and T13 represent an operator moving towards to bore of the scanner, along the central axis. Trajectories T3, T4, and T14 are similar, but a bit displaced (to avoid the examination couch and go towards the button panel embedded on the scanner).
- Trajectories T5 and T6 are translations performed near the side of the tubular scanner. Trajectory T6 maximizes the value of the magnetic field that can be experienced by the head in the lateral area. Moreover, T6 corresponds to a direction where the decay of the field is particularly strong.
- Trajectories T7 and T15 are  $180^\circ$  rotations of a person who is in front of the scanner and then turns to go away. Trajectories T8, T9 and T16 are similar, but with an off-centered starting position.
- Trajectories T10 and T16 describe an abrupt head rotation of a person who is facing the examination couch (and stays closed to it, supposing a width of 60 cm) and quickly turns to look inside the scanner. Note that, in Table 1, the minus sign in the path length of trajectories T10 and T16 indicates a clockwise rotation, opposite to the counterclockwise direction of the other ones.
- Trajectory T11 is a  $180^\circ$  rotation near the side of the tubular scanner, in the position that maximizes the value of the magnetic field when moving in the lateral area.

Note that all motions have a duration shorter than the time interval on which ICNIRP recommends to check the limit for the maximum variation of the flux density vector (3 s).

The maps of Fig.4 presents, for both scanners, the magnitude and direction of the flux density over a plane parallel to the floor, approximately at the height of the ears of model OM (i.e. 1.65 m above the floor), giving a general information about the exposure levels experienced by the body. If the heights of the other human models were considered, the maximum value of the magnetic flux density near the tubular scanner would change from 1.70 T to 4.20 T (for model SM) or 1.14 T (for model TM), whereas near the open scanner it would change from 1.60 T to 2.34 T (model SM) and 1.78 T (model TM). On the basis of these data, the



highest exposure indexes are expected for model SM. Note that values higher than the nominal induction (3 T for the tubular scanner, 1 T for the open one) can be found in close proximity to the coils, but they should not be accessible to the operators. The values of the magnetic flux density along the lateral side of the tubular scanner are quite lower than the values that can be found near the examination couch of both scanner; thus, relatively low exposure indexes are expected for movements performed in this area.

## RESULTS

This section presents the results of the exposure assessment, in terms of both indexes  $|\Delta\mathbf{B}|$  and  $EI$ . The analysis is focused on the head (starting just below the chin); hence, the number of considered voxels reduces to 71198.

### Maximum variation of the magnetic flux density vector

In all the 51 analyzed situations (i.e. combination of 17 trajectories and 3 model heights), the limit for the maximum variation of the magnetic flux density vector is never violated. The worst case is combination SM-T2 (near the tubular scanner), where the maximum  $|\Delta\mathbf{B}|$  is 1.39 T (i.e. less than 70 % of the limit). For the open scanner, the highest  $|\Delta\mathbf{B}|$  results to be 0.88 T (i.e. 44 % of the limit), obtained for combination SM-T13.

### Exposure index for the motion-induced electric field

The exposure index for the motion-induced electric field has been computed within the head, with both the DFT technique and the filter whose transfer function is described by Eq. 4. Moreover, the evaluation has been performed both including and excluding the DC component of the induced electric fields.

Table 2 provides, for all cases, the maximum value of  $EI$  obtained by including the DC component in the computations. The same table also presents, between brackets, the maximum value of  $EI$  obtained inside the central nervous system (CNS) of the head, composed of grey matter (9339 voxels), white matter (8215 voxels), cerebellum (2357 voxels), hippocampus (143 voxels), hypophysis (12 voxels), hypothalamus (5 voxels), medulla oblongata (57 voxels), midbrain (228 voxels), pinealbody (2 voxels), pons (262 voxels) and thalamus (30 voxels).

For all critical cases, Table 3 indicates the number of voxels where  $EI > 1$ , as well as the tissue they belong to. The corresponding results, obtained by excluding the DC component of the electric field from the analysis, are collected in Tables 4 and 5.

## DISCUSSION AND CONCLUSIONS

The simulations indicate that a violation of the limit for the maximum  $|\Delta\mathbf{B}|$  is quite unlikely, even in those cases (like rotations T7 and T15) where the body experiences the reversal of some field components. Other simulations (not reported for brevity), have shown that compliance with the basic restrictions for vertigo would be broken if the human model could go more close to the coils (e.g. extending trajectories T2 and T13 of further 10 cm beyond the final positions given in Table 1, to meet the highest field values reported in Fig.4). Even if the external cover of the scanners should not allow such position, these results suggest that the limit

could be violated if the operator put the head inside the bore of the tubular scanner or between the two poles of the open scanner.

The reported values of  $|\Delta B|$  would not change if higher speeds were adopted. On the contrary, for a given field distribution, the maximum  $|\Delta B|$  could be linearly increased with the nominal flux density of the scanner (but the values adopted in this study are the highest that can be commonly found in clinical environments).

The analysis of the exposure index for the electric field starts by considering the results obtained including the DC component in the weighted-peak approach (Tables 2 and 3). A general good agreement has been found between the DFT and the filter techniques, even if some significant deviations can occur in specific cases (see for example combination SM-T8 in Table 2). In about one half of the cases, the exposure index is higher when computed via DFT and vice versa for the other half. These discrepancies can be fully explained recalling that the DFT technique implements the ICNIRP limits directly, whereas the filter is an approximation (see Fig.1). Indeed, a dedicated analysis, not reported for brevity, has shown that the two techniques provide almost identical results if the harmonic spectra given by the DFT are “weighted” in frequency domain by adopting the magnitude and phase of the transfer function of the filter evaluated at the corresponding frequencies.

Despite the application to all tissues of the (more severe) limits for CNS, only seven of the 51 analyzed situations give  $EI > 1$  when the evaluation is performed through the filter; this number reduces to six when using the DFT (moreover, in combination SM-T2, the only material where  $EI > 1$  is the internal air, which is irrelevant). In most of such “critical” cases, the exposure index is higher than 1 in the CNS (in particular, for combinations OM-T10 and SM-T17, the absolute maximum of  $EI$  falls within the CNS itself). Other critical cases showing  $EI < 1$  in CNS (SM-T2 and TM-T17 computed with the filter) could have been over-penalized by the application of the limits for CNS everywhere. Note that the Guidelines for low-frequency fields (26) would require the comparison between the basic restrictions and the 99<sup>th</sup> percentile (instead of the local maximum) of the electric field. If this rule (here not adopted because not required by the Guidelines for motion-induced fields (1)) had been applied to the exposure index, none of the 51 analyzed situations would have produced a violation of the limits.

For both scanners, the case of the abrupt head rotation in proximity to the bore (trajectories T10 and T17) produces the highest exposure indexes. More in general, as expected, quite high exposure indexes are associated to trajectories where the body moves close to the tomograph (e.g. T2 and T13). This confirms what appears as a “natural” safety measure: to avoid positions in close proximity to the bore and to reduce the speed of motion. For most trajectories, model SM experiences the highest values of  $EI$ , whilst the lowest values are obtained with model TM (whose head is farther from the central axis of the scanners). For instance, making reference to trajectory T17, there is a ratio higher than 4 between the maximum exposure indexes computed in the CNS of models SM and TM. Moreover, the number of situations where the absolute maximum  $EI$  falls within the CNS reduces passing from model SM to TM. These data confirm the results of a previous study (30), where it was shown that the increase of the vertical distance between the head of the operator and the axis of a tubular scanner (e.g. by using elevation platforms or scanners embedded into the ground floor) can lead to significant reduction of the exposure levels.

The exposure index would scale linearly with the nominal flux density of the scanners (provided that the field distribution keeps the same), but it does not show a linear relation with the speed. Indeed, for a given path, a different speed value introduces a direct scaling on the magnitude of the induced field, but implies also a different duration of the induced signal, which in turn reflects on its harmonic content. Since the allowed limits reduce between 0.66 Hz and 25 Hz, a speed increment in many cases would give rise to a more than linearly increased exposure index, and vice versa. As an example, combinations SM-T10 and SM-T17 (i.e. the two 90° abrupt head rotations, representing the worst cases for the two scanners) have been simulated again, reducing the maximum angular speed (6.23 rad/s) by a factors 2/3 (4.15 rad/s) or 1/3 (2.08 rad/s). This operation has been done keeping the same speed profile and rotation angle, hence obtaining a prolongation of the duration from 0.3 s to 0.45 s or 0.9 s. The maximum exposure index given by the DFT technique decreases from 2.56 to 1.20 (i.e. 47%) or 0.38 (i.e. 15%) for combination SM-T10, and from 1.65 to 0.75 (i.e. 45%) or 0.21 (i.e. 13%) for combination SM-T17. Similar ratios are obtained by repeating the analysis through the filter, showing for both weighting techniques that a speed reduction corresponds to a more than linearly reduced exposure index.

In general, for the cases where the exposure index is sensibly larger than 1, the number of voxels exceeding the threshold results to be higher, confirming an higher probability of biological effect. On the contrary, when the exposure index is just slightly above the threshold (e.g. in case TM-T17 with the filter), the number of involved voxels is quite limited and therefore the biological effects should not be considered very likely to happen.

When analyzing the results obtained excluding the DC component of the electric field from the computation (Tables 4 and 5), almost all comments developed up to now keep their validity (at least qualitatively) and therefore they are not repeated. What is interesting to note is that, if the DC component is omitted, the exposure index may decrease, keep the same, or increase, depending on the specific case under analysis. For instance, referring to the DFT technique, the value of *EI* would reduce from 2.56 to 2.22 for combination SM-T10, but it would increase from 1.65 to 1.84 for combination SM-T17. This latter result is not surprising, because the weighted-peak approach does not quantify the energy of the induced signal (which should be evaluated over the whole time window and reduces whenever any harmonic component is removed from the spectrum), but focuses the attention on an instantaneous value (the peak of the weighted signal). In case of an induced signal with a positive DC component and a negative peak, the suppression of the DC component leads to an increase of both the (negative) peak and the final exposure index (always positive, owing to the square in Eq. 2).

If the attention is restricted to the critical cases, the comparison between Table 2 and Table 4 shows that they are the same, with the only exception given by combination TM-T17 evaluated with the DFT technique. This latter case has an exposure index lower than 1 if the DC component is taken into account, but it exceeds the limit when the DC component is excluded. Such a result proves the importance of removing from the Guidelines any possible element of ambiguity, making a specific discussion about this issue desirable in future versions of the Guidelines.

## APPENDIX

The filter used to perform the weighting in time domain is a dynamic system and its response may be affected by some transient effects, needed to ensure the continuity of the internal state variables. As already mentioned in other dosimetric studies based on the weighted-peak approach (31), this behavior can reflect on the computation of the exposure index.

In order to put in evidence the problem, a specific analysis is here developed with reference to a meaningful example, obtained when processing combination SM-T8. For the sake of clarity, only one component of the electric field (the main one) is analyzed. Figure 5 shows the time behavior of such an electric field component in the considered voxel (black curve). As can be seen, the signal starts and ends at zero level, and shows a significant DC component (about 0.104 V/m). If this DC component is removed before filtering, at the first instant the filter receives in input a discontinuous signal (passing abruptly from 0 to -0.104 V/m) and produces an output (red curve, in Fig.5) with a quite strong overshoot (-0.966 in dimensionless units). Apart from the sign, this overshoot would coincide with the exposure index. On the contrary, if the electric field signal is directly applied as an input for the filter, the transient effect due to the discontinuity is not present and the filter produces an output having a DC component equal to 0.0644. When such DC component is subtracted from the output signal, the result, indicated as a blue curve in Fig.5, has a peak of -0.292 at 40 ms, which, apart from the sign, gives the value of the exposure index. Note that, if the DC component of the signal were included in the computation, the peak of the signal would be at 200 ms, with a positive value equal to 0.336.

It must be noted that the overshoots in the response of the filter are due to discontinuities in the input signal, and not to the DC component in itself. Thus, the same problem would be present also in case of trajectories that involve some discontinuity in the speed profile, proving the importance of simulating it in a quite realistic way.

The problem of the anomalous overshoot does not occur when filtering in frequency domain via DFT, neither removing the DC component before, nor after, the weighting. However, the weighting based on DFT can give rise to some arbitrariness too. Indeed, as known from the theory of Fourier Transform, the harmonics computed through a DFT represent the coefficient of the periodic continuation of the original signal. Thus, the weighting based on DFT actually does not operate on the real induced signal (which typically is aperiodic), but on its periodic extension. This feature inherently introduces some degrees of freedom in the computation of the exposure index due to the choice of the observation time window where the DFT is applied (see a specific example discussed in (32)).

Table 1

Features of the considered trajectories

Scanner	Trajectory	Type	Starting point	Final Point	Path length	Duration	Maximum speed
Tubular	T1	Translation	$x = 1.1 \text{ m}$ $z = 1.2 \text{ m}$	$x = -1.1 \text{ m}$ $z = 1.2 \text{ m}$	2.2 m	2 s	1.22 m/s
	T2	Translation	$x = 0$ $z = 2.05 \text{ m}$	$x = 0 \text{ m}$ $z = 1.05 \text{ m}$	1 m	1 s	1.19 m/s
	T3	Translation	$x = 0.5 \text{ m}$ $z = 2.05 \text{ m}$	$x = 0.5 \text{ m}$ $z = 1.05 \text{ m}$	1 m	1 s	1.19 m/s
	T4	Translation	$x = 0.9 \text{ m}$ $z = 2.05 \text{ m}$	$x = 0.9 \text{ m}$ $z = 1.05 \text{ m}$	1 m	1 s	1.19 m/s
	T5	Translation	$x = 1.3 \text{ m}$ $z = -0.85 \text{ m}$	$x = 1.3 \text{ m}$ $z = 0.85 \text{ m}$	1.7 m	1.6 s	1.20 m/s
	T6	Translation	$x = 1.15 \text{ m}$ $z = 0.5 \text{ m}$	$x = 2.15 \text{ m}$ $z = 0.5 \text{ m}$	1 m	1 s	1.19 m/s
	T7	Rotation	$x = 0$ $z = 1.2 \text{ m}$	-	180°	1 s	3.74 rad/s
	T8	Rotation	$x = 0.5 \text{ m}$ $z = 1.2 \text{ m}$	-	180°	1 s	3.74 rad/s
	T9	Rotation	$x = 0.9 \text{ m}$ $z = 1.2 \text{ m}$	-	180°	1 s	3.74 rad/s
	T10	Rotation	$x = 0.3 \text{ m}$ $z = 1.2 \text{ m}$	-	-90°	0.3 s	6.23 rad/s
	T11	Rotation	$x = 1.3 \text{ m}$ $z = 0.5 \text{ m}$	-	180°	1 s	3.74 rad/s
Open	T12	Translation	$x = 1.1 \text{ m}$ $y = -1.3 \text{ m}$	$x = -1.1 \text{ m}$ $y = -1.3 \text{ m}$	2.2 m	2 s	1.22 m/s
	T13	Translation	$x = 0$ $y = -2.15 \text{ m}$	$x = 0$ $y = -1.15 \text{ m}$	1 m	1 s	1.19 m/s
	T14	Translation	$x = 0.5 \text{ m}$ $y = -2.15 \text{ m}$	$x = 0.5 \text{ m}$ $y = -1.15 \text{ m}$	1 m	1 s	1.19 m/s
	T15	Rotation	$x = 0$ $y = -1.3 \text{ m}$	-	180°	1 s	3.74 rad/s
	T16	Rotation	$x = 0.5 \text{ m}$ $y = -1.3 \text{ m}$	-	180°	1 s	3.74 rad/s
	T17	Rotation	$x = 0.3 \text{ m}$ $y = -1.3 \text{ m}$	-	-90°	0.3 s	6.23 rad/s

Table 2

Maximum exposure index in the head and in the CNS, computed including the DC component of the induced signals

Trajectory	SM ( $h = 1.62$ m)		OM ( $h = 1.77$ m)		TM ( $h = 1.92$ m)	
	DFT	Filter	DFT	Filter	DFT	Filter
T1	0.51 (0.31)	0.45 (0.28)	0.23 (0.17)	0.22 (0.16)	0.12 (0.09)	0.13 (0.10)
T2	1.38* (0.81)	1.19* (0.73)	0.63 (0.63)	0.58 (0.58)	0.51 (0.51)	0.47 (0.47)
T3	0.61 (0.60)	0.57 (0.57)	0.60 (0.60)	0.52 (0.52)	0.36 (0.36)	0.32 (0.32)
T4	0.41 (0.30)	0.36 (0.27)	0.28 (0.16)	0.25 (0.14)	0.15 (0.08)	0.14 (0.07)
T5	0.27 (0.20)	0.22 (0.15)	0.19 (0.13)	0.15 (0.10)	0.13 (0.08)	0.10 (0.06)
T6	0.33 (0.32)	0.32 (0.30)	0.22 (0.19)	0.21 (0.18)	0.13 (0.11)	0.13 (0.10)
T7	0.70 (0.23)	0.69 (0.25)	0.22 (0.22)	0.24 (0.24)	0.31 (0.31)	0.35 (0.35)
T8	0.52 (0.37)	0.41 (0.41)	0.35 (0.33)	0.40 (0.40)	0.30 (0.25)	0.31 (0.29)
T9	0.26 (0.22)	0.27 (0.23)	0.20 (0.15)	0.22 (0.16)	0.15 (0.10)	0.16 (0.10)
T10	2.56* (1.43*)	2.43* (1.84*)	1.40* (1.40*)	1.58* (1.58*)	1.32* (1.10*)	1.44* (1.24*)
T11	0.17 (0.13)	0.13 (0.12)	0.12 (0.09)	0.10 (0.08)	0.08 (0.06)	0.06 (0.05)
T12	0.10 (0.10)	0.09 (0.09)	0.09 (0.07)	0.09 (0.06)	0.05 (0.04)	0.06 (0.04)
T13	0.80 (0.80)	0.76 (0.76)	0.69 (0.64)	0.62 (0.57)	0.56 (0.31)	0.47 (0.29)
T14	0.37 (0.37)	0.35 (0.35)	0.30 (0.30)	0.28 (0.28)	0.24 (0.15)	0.21 (0.15)
T15	0.50 (0.50)	0.57 (0.57)	0.48 (0.34)	0.48 (0.38)	0.28 (0.10)	0.27 (0.10)
T16	0.33 (0.33)	0.32 (0.32)	0.26 (0.25)	0.28 (0.24)	0.17 (0.10)	0.19 (0.10)
T17	1.65* (1.65*)	1.94* (1.94*)	1.59* (1.12*)	1.77* (1.33*)	0.97 (0.36)	1.08* (0.41)

\* $EI > 1$ 

Table 3

Tissues and number of voxels with  $EI > 1$ , determined including the DC component of the induced signals

Case	DFT	Filter
SM-T2	Internal Air (9)	Internal Air (4)
SM-T10	Internal Air (35), Grey Matter (9), Fat (5), Subcutaneous Fat (19), Ear Skin (54), Skull (15)	Internal Air (63), Grey Matter (16), Fat (5), Subcutaneous Fat (25), Ear Skin (75), Skull (35)
OM-T10	Internal Air (2), Grey Matter (5), Ear Skin (9), Skull (4)	Internal Air (9), Grey Matter (6), Ear Skin (14), Skull (5)
TM-T10	Grey Matter (2), Ear Skin (9)	Internal Air (4), Grey Matter (2), Ear Skin (16), Skull (4)
SM-T17	Internal Air (26), Grey Matter (16), Subcutaneous Fat (2), Ear Skin (25), Skull (21)	Internal Air (44), Grey Matter (31), Fat (1), Muscle (1), Subcutaneous Fat (4), Ear Skin (38), Skull (51)
OM-T17	Internal Air (1), Grey Matter (1), Ear Skin (15), Skull (1)	Internal Air (13), Grey Matter (1), Subcutaneous Fat (3), Ear Skin (20), Skull (5)
TM-T17	-	Ear Skin (5)

Table 4

Maximum exposure index in the head and in the CNS, computed excluding the DC component of the induced signals

Trajectory	SM ( $h = 1.62$ m)		OM ( $h = 1.77$ m)		TM ( $h = 1.92$ m)	
	DFT	Filter	DFT	Filter	DFT	Filter
T1	0.50 (0.31)	0.45 (0.28)	0.24 (0.17)	0.23 (0.16)	0.12 (0.09)	0.13 (0.09)
T2	1.55* (0.89)	1.33* (0.80)	0.70 (0.70)	0.64 (0.64)	0.56 (0.56)	0.50 (0.50)
T3	0.71 (0.67)	0.64 (0.62)	0.64 (0.64)	0.56 (0.56)	0.40 (0.40)	0.33 (0.33)
T4	0.44 (0.34)	0.38 (0.29)	0.30 (0.19)	0.25 (0.15)	0.17 (0.10)	0.14 (0.09)
T5	0.26 (0.19)	0.21 (0.14)	0.18 (0.12)	0.14 (0.09)	0.12 (0.07)	0.09 (0.06)
T6	0.30 (0.29)	0.29 (0.27)	0.20 (0.17)	0.19 (0.16)	0.12 (0.10)	0.11 (0.09)
T7	0.70 (0.20)	0.69 (0.22)	0.20 (0.20)	0.22 (0.22)	0.28 (0.28)	0.31 (0.31)
T8	0.41 (0.41)	0.44 (0.44)	0.33 (0.32)	0.39 (0.38)	0.31 (0.23)	0.32 (0.26)
T9	0.25 (0.19)	0.27 (0.20)	0.19 (0.13)	0.21 (0.13)	0.14 (0.08)	0.15 (0.08)
T10	2.22* (1.38*)	2.14* (1.78*)	1.53* (1.53*)	1.68* (1.68*)	1.39* (1.26*)	1.50* (1.37*)
T11	0.14 (0.12)	0.14 (0.14)	0.10 (0.08)	0.09 (0.09)	0.07 (0.05)	0.06 (0.06)
T12	0.10 (0.10)	0.09 (0.09)	0.09 (0.07)	0.09 (0.06)	0.05 (0.04)	0.06 (0.04)
T13	0.88 (0.88)	0.83 (0.83)	0.76 (0.71)	0.68 (0.63)	0.62 (0.34)	0.50 (0.30)
T14	0.43 (0.43)	0.39 (0.39)	0.34 (0.34)	0.31 (0.31)	0.27 (0.18)	0.22 (0.16)
T15	0.46 (0.45)	0.51 (0.51)	0.48 (0.30)	0.47 (0.34)	0.28 (0.10)	0.27 (0.09)
T16	0.33 (0.33)	0.32 (0.32)	0.28 (0.24)	0.30 (0.23)	0.19 (0.10)	0.20 (0.10)
T17	1.84* (1.84*)	2.09* (2.09*)	1.70* (1.26*)	1.86* (1.45*)	1.04* (0.42)	1.14* (0.46)

\* $EI > 1$

Table 5

Tissues and number of voxels with  $EI > 1$ , determined excluding the DC component of the induced signals

Case	DFT	Filter
SM-T2	Internal Air (15)	Internal Air (12)
SM-T10	Internal Air (16), Grey Matter (5), Subcutaneous Fat (15), Ear Skin (45), Skull (8)	Internal Air (39), Grey Matter (14), Fat (2), Subcutaneous Fat (21), Ear Skin (69), Skull (19)
OM-T10	Internal Air (5), Grey Matter (4), Ear Skin (9), Skull (3)	Internal Air (11), Grey Matter (6), Ear Skin (14), Skull (6)
TM-T10	Internal Air (3), Grey Matter (1), Ear Skin (11), Skull (3)	Internal Air (11), Grey Matter (4), Subcutaneous Fat (1), Ear Skin (20), Skull (8)
SM-T17	Internal Air (38), Grey Matter (23), Fat (1), Subcutaneous Fat (3), Ear Skin (30), Skull (29)	Internal Air (61), Grey Matter (38), Fat (2), Muscle (1), Subcutaneous Fat (5), Ear Skin (44), Skull (59)
OM-T17	Internal Air (8), Grey Matter (1), Subcutaneous Fat (1), Ear Skin (18), Skull (3)	Internal Air (20), Grey Matter (5), Subcutaneous Fat (4), Ear Skin (26), Skull (7)
TM-T17	Ear Skin (2)	Ear Skin (7)

## ACKNOWLEDGMENTS

This work received funding from the European Metrology Research Programme (EMRP)-HLT06 Joint Research Project (JRP) “Metrology for next-generation safety standards and equipment in MRI” (2012–2015). EMRP is jointly funded by the EMRP participating countries within EURAMET and the European Union. The authors wish to acknowledge Dr. D. Giordano and Dr. G. Bordonaro for useful discussions and contributions.

## REFERENCES

1. International Commission on Non-Ionizing Radiation Protection. Guidelines for limiting exposure to electric fields induced by movement of the human body in a static magnetic field and by time-varying magnetic fields below 1 Hz. *Health Phys.* 2014;106:418–425.
2. International Commission on Non-Ionizing Radiation Protection. Guidelines on limits of exposure to static magnetic fields. *Health Phys.* 2009;96:504–514.
3. Heinrich A, Szostek A, Nees F, Meyer P, Semmler W, Flor H. Effects of static magnetic fields on cognition, vital signs, and sensory perception: A meta-analysis. *J. Magn. Reson. Im.* 2011;34:758–763.
4. Friebe B, Wollrab A, Thormann M, Fischbach K, Ricke J, Grueschow M, Kropf S, Fischbach F, Speck O. Sensory perceptions of individuals exposed to the static field of a 7T MRI: A controlled blinded study. *J. Magn. Reson. Im.* Early view. DOI 10.1002/jmri.24748.
5. Glover PM, Cavin I, Qian R, Bowtell R, Gowland PA. Magnetic field-induced vertigo: a theoretical and experimental investigation. *Bioelectromagnetics.* 2007;28:349–361.
6. Cavin ID, Glover PM, Bowtell RW, Gowland PA. Thresholds for perceiving metallic taste at high magnetic field. *J. Magn. Reson. Im.* 2007;26:1357–1361.
7. Schenck JF, Dumoulin CL, Redington RW, Kressel HY, Elliott RT, McDougall IL. Human exposure to 4.0-Tesla magnetic fields in a whole-body scanner. *Med. Phys.* 1992;19:1089–98.
8. De Vocht F, Van Wendelde-Joode B, Engels H, Kromhout H. Neurobehavioral effects among subjects exposed to high static and gradient magnetic fields from a 1.5 tesla magnetic resonance imaging system—a case-crossover pilot study. *Magn. Reson. Med.* 2003;50:670–674.
9. Rata M, Birlea V, Murillo A, Paquet C, Cotton F, Salomir R. Endoluminal MR-guided ultrasonic applicator embedding cylindrical phased-array transducers and opposed-solenoid detection coil. *Magn. Reson. Med.* 2015;73:417–426.
10. McVeigh ER, Guttman MA, Lederman RJ, Li M, Kocaturk O, Hunt T, Kozlov S, Horvath KA. Real-time interactive MRI-guided cardiac surgery: aortic valve replacement using a direct apical approach. *Magn. Reson. Med.* 2006;56:958–964.
11. Schaap K, Christopher-De Vries Y, Cambron-Goulet E, Kromhout H. Work-Related Factors Associated with Occupational Exposure to Static Magnetic Stray Fields from MRI Scanners. *Magn. Reson. Med.* 2015. doi: 10.1002/mrm.25720.
12. Bongers S, Slottje P, Portengen L, Kromhout H. Exposure to Static Magnetic Fields and Risk of Accidents among a Cohort of Workers from a Medical Imaging Device Manufacturing Facility. *Magn. Reson. Med.* 2015. doi: 10.1002/mrm.25768.
13. Liu F, Zhao H, Crozier S. Calculation of electric fields induced by body and head motion in high-field MRI. *J. Magn. Reson.* 2003;161:99–107.
14. Crozier S, Liu F. Numerical evaluation of the fields induced by body motion in or near high-field MRI scanners. *Progr. Biophys. Molec. Biol.* 2005;87:267–278.



15. Wang H, Trakic A, Liu F, Crozier S. Numerical field evaluation of healthcare workers when bending towards high-field MRI magnets. *Magn. Reson. Med.* 2008;59:410–422.
16. Ilvonen S, Laakso I. Computational estimation of magnetically induced electric fields in a rotating head. *Phys. Med. Biol.* 2009;54:341–351.
17. Cobos Sanchez C, Bowtell RW, Power H, Glover P, Marin L, Becker AA, Jones A. Forward electric field calculation using BEM for time-varying magnetic field gradients and motion in strong static fields. *Eng. Anal. Bound. Elem.* 2009;33:1074–1088.
18. Chiampi M, Zilberti L. Induction of Electric Field in Human Bodies Moving Near MRI: an Efficient BEM Computational Procedure. *IEEE Trans. Biom. Eng.* 2011;58:2787–2793.
19. Jokela K, Saunders RD. Physiologic and dosimetric considerations for limiting electric fields induced in the body by movement in a static magnetic field. *Health Phys.* 2011;100:641–653.
20. Cobos-Sanchez C, Glover P, Power H, Bowtell RW. Calculation of the electric field resulting from human body rotation in a magnetic field. *Phys. Med. Biol.* 2012;57:4739–4753.
21. Zilberti L, Chiampi M. A Numerical Survey of Motion-Induced Electric Fields Experienced by MRI Operators. *Health Phys.* 2013;105:498–511.
22. Laakso I, Kannala S, Jokela K. Computational dosimetry of induced electric fields during realistic movements in the vicinity of a 3 T MRI scanner. *Phys. Med. Biol.* 2013;58:2625–2640.
23. Trakic A, Liu L, Sanchez-Lopez H, Zilberti L, Liu F, Crozier S. Numerical safety study of currents induced in the patient during rotations in the static field produced by a hybrid MRI-LINAC system. *IEEE Trans. Biom. Eng.* 2014;61:784–793.
24. Zilberti L, Bottauscio O, Chiampi M. Motion-induced fields in MRI: are the dielectric currents really negligible?. *IEEE Magnetics Letters.* 2015;6:1500104.
25. European Parliament. Directive 2013/35/EU of the European Parliament and of the Council of 26 June 2013 on the minimum health and safety requirements regarding the exposure of workers to the risks arising from physical agents (electromagnetic fields) (20th individual Directive within the meaning of Article 16(1) of Directive 89/391/EEC) and repealing Directive 2004/40/EC. Available at: <http://eur-lex.europa.eu/homepage.html>. Accessed April 30, 2015.
26. International Commission on Non-Ionizing Radiation Protection. Guidelines for limiting exposure to time-varying electric and magnetic fields (1 Hz to 100 kHz). *Health Phys.* 2010;99:818–836.
27. Christ A, Kainz W, Hahn EG, et al. The Virtual Family-development of surface-based anatomical models of two adults and two children for dosimetric simulations. *Phys. Med. Biol.* 2010;55:N23–N38.
28. Hasgall PA, Di Gennaro F, Baumgartner C, Neufeld E, Gosselin MC, Payne D, Klingensböck A, Kuster N. IT'IS Database for thermal and electromagnetic parameters of biological tissues. <http://www.itis.ethz.ch/database>. Version 2.6, January 2015. Accessed April 30, 2015.

29. International Commission on Non-Ionizing Radiation Protection. Guidance on determining compliance of exposure to pulsed and complex non-sinusoidal waveforms below 100 kHz with ICNIRP guidelines. Health Phys. 2003;84:383–387.
30. Trakic A, Wang H, Liu F, Sanchez-Lopez H, Weber E, Crozier S. Minimizing the Induced Fields in MRI Occupational Workers by Lowering the Imager. Concept. Magn. Reson. B. 2008;33B:39–54.
31. Crotti G, Giordano D. Analysis of critical situations in the evaluation of human exposure to magnetic fields with complex waveforms. Radiat. Prot. Dosim. 2009;137:227-230.
32. Zilberti L, Bottauscio O, Chiampi M. A Potential-based Formulation for Motion-Induced Electric Fields in MRI. To appear on IEEE T. Magn. DOI: 10.1109/TMAG.2015.2474748.

## LIST OF FIGURE CAPTIONS

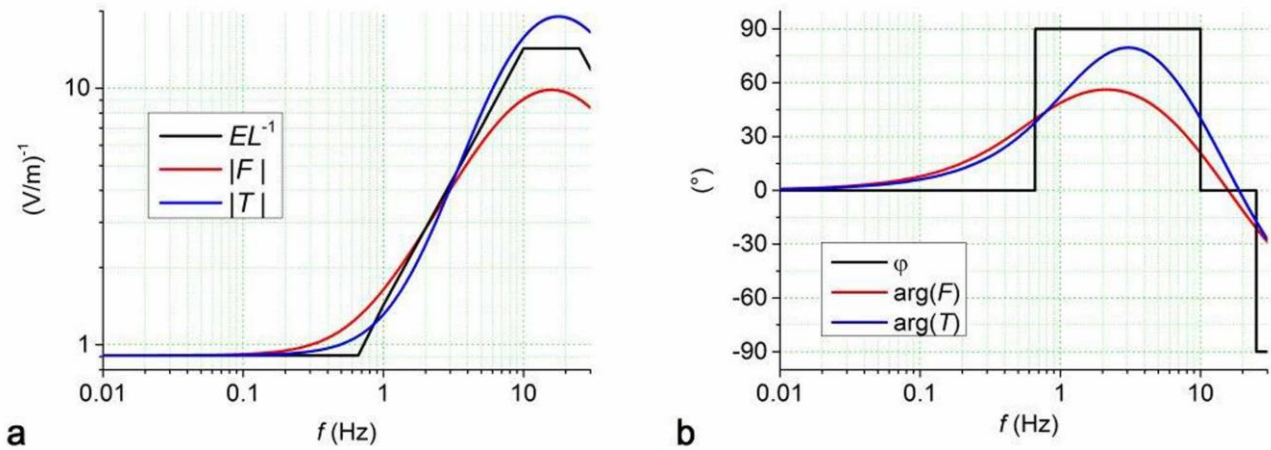


FIG.1. Comparison between the weighting function given in Eq. 1 and those realized by the filters: magnitude (a); phase (b).

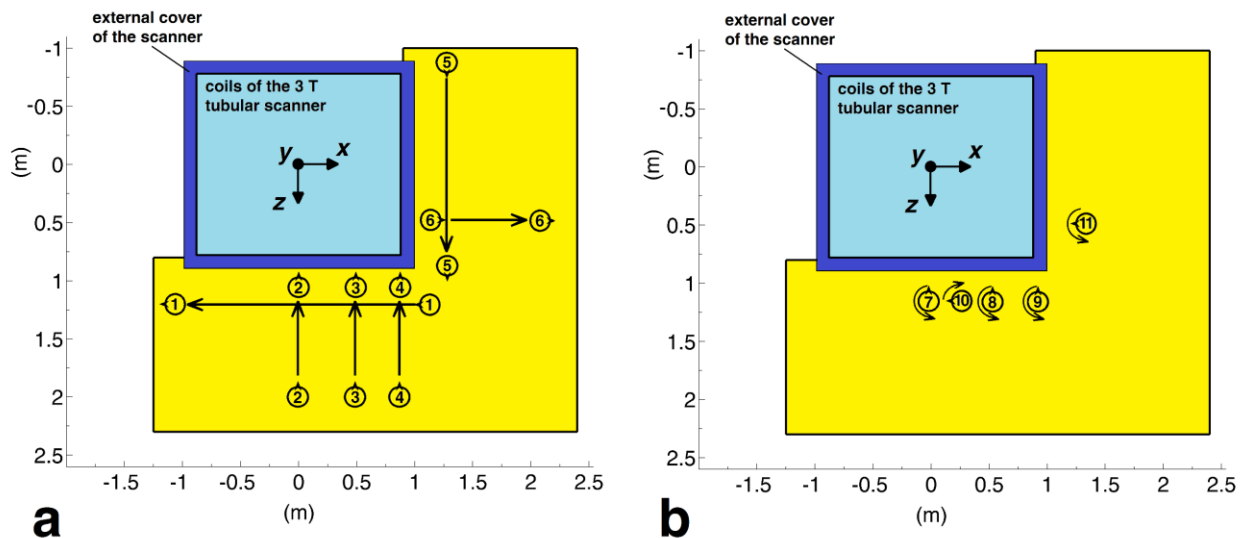


FIG.2. Schematic top-view of the trajectories considered for the exposure scenario with tubular scanner: translations (a); rotations (b).

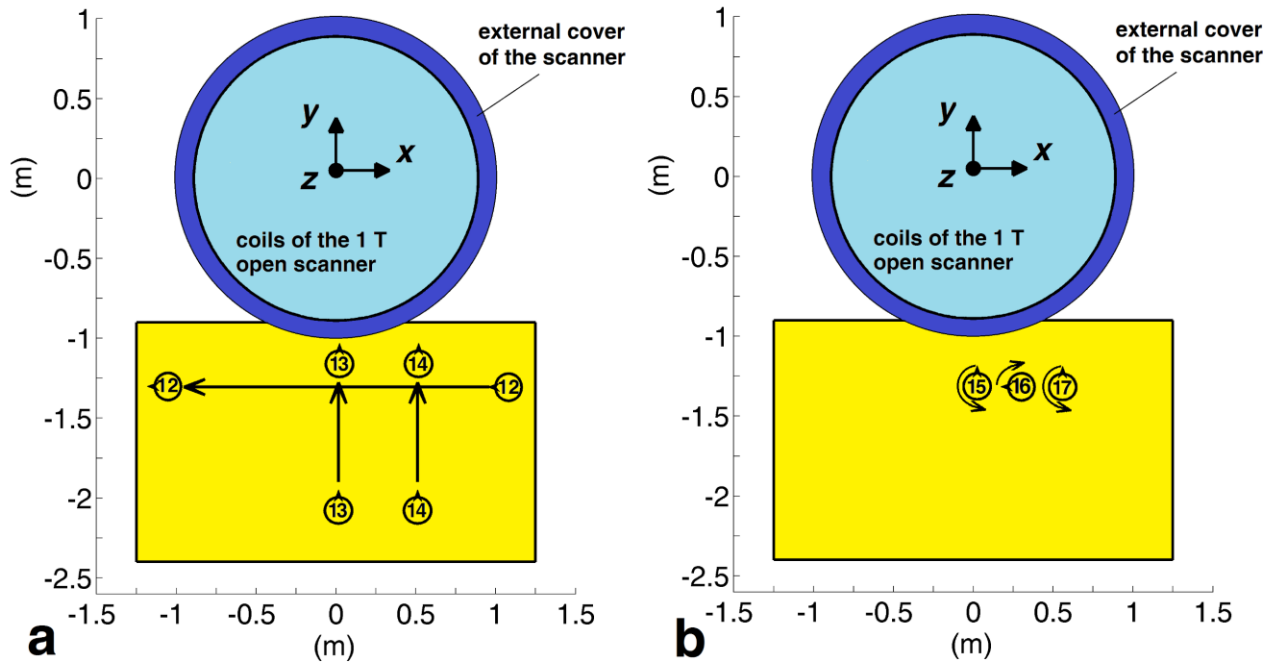


FIG.3. Schematic top-view of the trajectories considered for the exposure scenario with open scanner: translations (a); rotations (b).

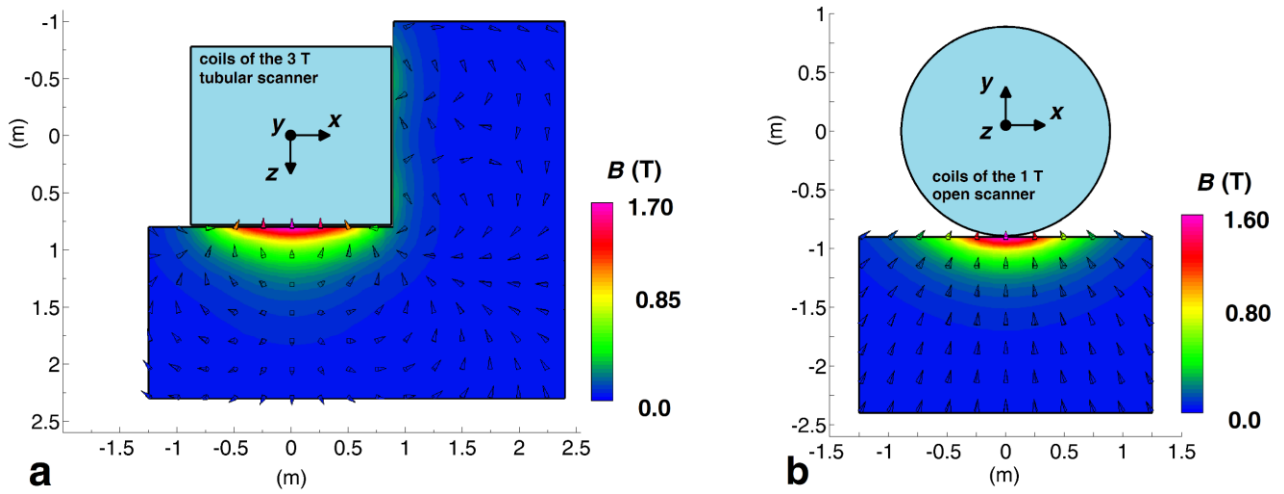


FIG.4. Magnitude of flux density over a plane 1.65 m above ground: tubular scanner (a); open scanner (b).

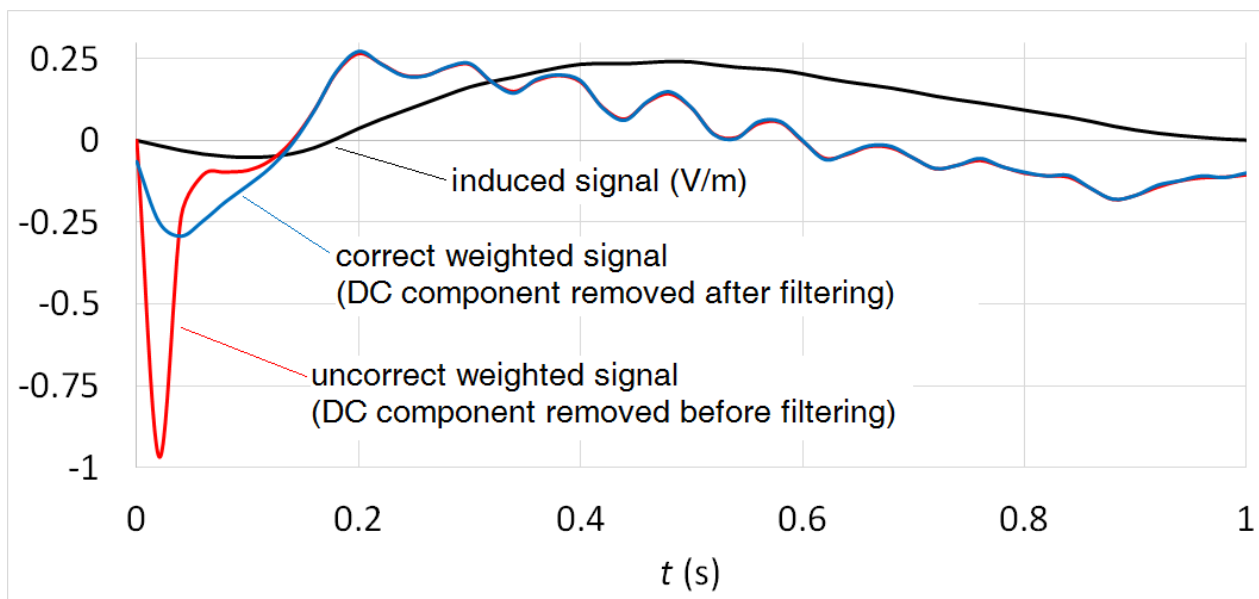


FIG.5. Example to show how to filter in time domain and remove the DC component from the computation of the exposure index.